Journal of Geophysical Research: Space Physics

RESEARCH ARTICLE
10.1029/2018JA025525

Quantifying the Sources of Ionosphere Day-To-Day Variability

Tzu-Wei Fang[1,2], Tim Fuller-Rowell[1], Valery Yudin[1], Tomoko Matsuo[3], and Rodney Viereck[4]

[1]Cooperative Institute for Research in Environmental Sciences, University of Colorado Boulder, Boulder, CO, USA, [2]Satellite Research Center, School of Electrical and Electronic Engineering, Nanyang Technological University, Singapore, [3]Ann and H. J. Smead Aerospace Engineering Sciences, University of Colorado Boulder, Boulder, CO, USA, [4]Space Weather Prediction Center, National Oceanic and Atmospheric Administration, Boulder, CO, USA

Key Points:
- Simulation reproduces reasonable day-to-day variability compared to previous observations
- Geomagnetic activity is the main contributor to the relative ionospheric variability
- Ionospheric variability shows significant longitudinal, latitudinal, and local time dependency

Correspondence to:
T.-W. Fang,
tzu-wei.fang@noaa.gov

Citation:
Fang, T.-W., Fuller-Rowell, T., Yudin, V., Matsuo, T., & Viereck, R. (2018). Quantifying the sources of ionosphere day-to-day variability. *Journal of Geophysical Research: Space Physics*, *123*, 9682–9696. https://doi.org/10.1029/2018JA025525

Received 27 MAR 2018
Accepted 11 OCT 2018
Accepted article online 17 OCT 2018
Published online 8 NOV 2018

Abstract Simulations from the coupled Whole Atmosphere Model and Global Ionosphere Plasmasphere show significant day-to-day variations in total electron content (TEC) and the *F* region peak density (N_mF_2). The Whole Atmosphere Model-Global Ionosphere Plasmasphere was driven by the auroral precipitation patterns inferred from TIROS/NOAA, daily solar irradiance measurements derived from the satellite observations, and 5-min interplanetary magnetic field/solar wind parameters during June and July 2012. Overall, the combination of solar, magnetosphere, and lower atmosphere drivers produced similar magnitude of variability consistent with that seen in observations. Results also show that the relative variability is much larger at night than in the daytime, due to much lower background density, and depended strongly on latitude and local time. Additional simulations were also performed to distinguish the contributions to the variability from solar activity, geomagnetic activity, and lower atmospheric perturbations. Results show that globally, geomagnetic activity is the main contributor to the N_mF_2 variability, followed by lower atmosphere perturbation, and then solar activity. For TEC variability, again, geomagnetic activity is the main contributor, followed by solar activity, and then lower atmosphere perturbation. In terms of absolute variability, at low latitudes solar activity dominates the TEC variability, most likely due to the importance of solar EUV driving the changes in ionosphere density through photoionization, while the contributions from the lower atmosphere and geomagnetic activity are almost equally. For the middle- and high-latitude regions, the solar activity and geomagnetic activity are the most important sources for the TEC variability.

1. Introduction

Establishing the capability of predicting the weather in the upper atmosphere and ionosphere remains one of the greatest challenges in the ionosphere-thermosphere (I-T) community. The largest difficulty is how to incorporate all the necessary physics in the first-principle model to accurately capture different scales of variabilities that are observed by ground-based and satellite measurements. Timescales of variability range from minutes to years and are driven by many different sources in the system. In general, ionospheric variability is caused by solar radiation, solar wind, geomagnetic and auroral activity, variation in the neutral atmosphere, and electrodynamic processes (Rishbeth & Mendillo, 2001). Phenomena that originate from the Sun, such as solar flares, solar cycle activity, and solar rotation, can impact the ionosphere through ionization processes, resulting in ionospheric variability with timescales from minutes to years. Strong geomagnetic storms lead to positive or negative ionospheric storms depending on season, local time, and the universal time (UT) arrival time of storms. Different scales of neutral atmosphere waves, such as gravity waves, thermospheric tides, and planetary waves, driven by lower atmosphere processes, can also influence the ionosphere directly through plasma transport or indirectly through electrodynamic processes. Thermospheric composition, temperature, and winds also respond to geomagnetic activity to further impact the ionosphere through chemical reactions and electrodynamics.

Under quiet geomagnetic conditions, the electrodynamics of the equatorial ionosphere are primarily determined by thermospheric neutral wind and ionospheric conductivity. Studies have shown that atmospheric tides and waves that are associated with terrestrial weather can significantly contribute to the pronounced day-to-day variability of the equatorial electric field especially under low solar activity and quiet geomagnetic conditions. The phases and magnitudes of migrating tides, in particular, the semidiurnal westward wave number 2 (SW2) tide, play an important role in driving the daytime equatorial electrodynamics (e.g., Fang et al., 2013; Millward et al., 2001). Nonmigrating tides, such as the diurnal

eastward wave number 3 (DE3) tide excited by the diurnal variation of convection and latent heat release from tropical topography, are capable of creating pronounced longitudinal structures at low-latitude ionosphere density (e.g., Hagan et al., 2007; Immel et al., 2006). When a major sudden stratospheric warming event happens, planetary waves and thermospheric tides can change dramatically and lead to a large modulation of equatorial electric fields in the low-latitude ionosphere (e.g., Chau et al., 2009; Fuller-Rowell et al., 2010; Goncharenko et al., 2010).

When geomagnetic activity increases, electrodynamic processes are further perturbed by the disturbance wind dynamo and a penetration electric field originating in the magnetosphere. After the onset time of a storm, the equatorial zonal electric fields can be significantly modulated by the prompt penetration electric fields from high latitudes caused by the rapid changes in the interplanetary electric field (IMF). During very large storms, these electric fields are substantially larger than the fields associated with the normal fountain effect. If IMF is southward, leading to a dawn-to-dusk or dayside eastward electric field, this superposed electric field will enhance the normal fountain effect greatly. This has been called the superfountain effect (e.g., Mannucci et al., 2005; Tsurutani et al., 2008). With the much larger electric fields, the dayside equatorial plasma is lifted up to much higher altitudes and latitudes than normal. It is generally believed that the penetration of electric fields can last only about 60 min after the onset time of a geomagnetic storm because of a shielding effect by the ring current system (e.g., Kikuchi et al., 1996). However, some observations indicate that the IMF can continuously penetrate to the low-latitude ionosphere without shielding for many hours as long as the strengthening of the magnetic activity is occurring under storm conditions (Huang et al., 2005). The prompt penetration electric fields effect strongly dominates the equatorial electric field during the main phase of magnetic storms. The storm-enhanced equatorward wind caused by high-latitude heating and the Coriolis force result in a strong westward wind at midlatitudes, which changes the global electric circuit in the ionosphere through the dynamo mechanism. The process has been referred as *disturbance dynamo* (Blanc & Richmond, 1980). Depending on the strength of the storm, disturbance dynamo can further impact the I-T system for 1 to 4 days after the main storm. The temporal and spatial variations of storm time equatorial electrodynamics strongly depend on the evolution of geomagnetic disturbance, the nature of the energy inputs to the ionosphere and thermosphere, and the response of ionospheric conductivity and thermospheric dynamics. The corresponding changes in the I-T system become much more complex, with the temporal and spatial variations of equatorial electric fields reflecting different physical processes occurring during geomagnetic storms (e.g., Fejer, 2002; Fuller-Rowell et al., 1994, 1997).

Taking advantage of long-term time series ionosonde records at multiple locations, several studies have been carried out aiming to reveal the variability of the *F* region ionosphere. Using a data set of f_oF_2 values during 1976–1989 from 100 ionosondes, Forbes et al. (2000) concluded that under quiet geomagnetic conditions ($K_p < 1$), the residual variability consists of about 25%–35% of high frequencies (periods of a few hours to 1–2 days) and about 15%–20% of low frequencies (periods of approximately 2–30 days) at all latitudes. Forbes et al. found little day-to-day correlations of these variabilities with $F_{10.7}$ and suggested that these variabilities are mainly due to meteorological influences at these frequencies. Rishbeth and Mendillo (2001) utilized 34 years (1957–1990) of observations from 13 ionosonde stations to extract timescales of ionospheric variability ranging from days to months. In studying day-to-day variability, they concluded that under moderate solar activity condition the N_mF_2 has a standard deviation of 20% during the day and 33% at night. Their study also suggested that the variability of N_mF_2 is largely contributed by the geomagnetic activity and partially by meteorological sources from the lower atmosphere. Araujo-Pradere et al. (2005) determined the variability of the *F* region as a function of local time, latitude, season, and geomagnetic activity using 75 ionosonde stations during 43 storm intervals. They concluded that during the storms the largest variability of N_mF_2 tends to occur in winter. At middle and low latitudes, the variability tends to increase with geomagnetic activity in winter and equinox but reminds fairly constant in summer. At high latitudes, the variability tends to decrease particularly in winter. Araujo-Pradere et al. also provided possible physical explanations for these seasonal variations in their study.

Recent development in whole atmosphere modeling has shed light on the possibility of reproducing the daily variability of the I-T system. Several Whole Atmosphere Models, such as the Whole Atmosphere Model (WAM) developed at NOAA Space Weather Prediction Center (SWPC), the Whole Atmosphere Community Climate Model with thermosphere and ionosphere extension (WACCM-X) built at National

Center for Atmospheric Research, and Ground-to-topside model of Atmosphere and Ionosphere for Aeronomy established at National Institute of Information and Communications Technology in Japan, are capable of reproducing fully coupled atmospheric dynamics from the Earth's surface all the way to the thermosphere. Parameterizations of solar heating/dissociation/ionization and empirical model of high-latitude electric fields are also implemented in WAM and WACCM-X to simulate the impact of solar and geomagnetic activity. Studies using WAM (Fang et al., 2013) and WACCM-X (Liu et al., 2013) have demonstrated that significant day-to-day variability in ionospheric density and equatorial vertical drift are captured by these models. Using WAM and WACCM-X under geomagnetic quiet and moderate solar activity conditions, their results also suggested that lower atmospheric perturbations account for about half of the day-to-day ionospheric variability. WAM development, in particular, is largely supported by NOAA SWPC and aims to provide upper atmosphere predictions for space weather operations. To be able to precisely capture the variability from different sources using the WAM becomes one of the most important criteria that needs to be considered during the evaluation process.

Building upon the Fang et al. (2013) study, simulations were performed using the one-way coupled WAM and Global Ionosphere Plasmasphere (GIP) model, with realistic solar and geomagnetic activity for a 2-month period. The first goal of this study is to demonstrate the amount of ionospheric variability that can be captured using the state-of-the-art model with realistic drivers from the Sun, geomagnetic activity, and lower atmospheric tides/waves. The second goal is to quantify the relative contribution of solar radiation, geomagnetic, and lower atmosphere dynamics in the different regions. The second goal is achieved by removing one or two sources of variability from the simulations. In this paper, we introduce the numerical models used for our study and describe our recent implementations in section 2, summarize our findings of ionospheric variability captured in our simulation, and quantify the sources of these variabilities in section 3, and the final conclusion is provided in section 4.

2. Model Simulation

The WAM (Akmaev et al., 2008; Fuller-Rowell, Akmaev, et al., 2008) is a general circulation model for the neutral atmosphere. WAM is an extension of the operational Global Forecast System (GFS) model used by the U.S. National Weather Service for weather prediction to include the upper atmosphere. The code was extended from the original 64 layers in GFS to 150 layers, with the top pressure level raised from 64 (~55 km) to 3×10^{-7} Pa (~600 km) with layer thickness of a quarter-scale height in the stratosphere, mesosphere, and thermosphere. It treats the thermospheric major species O, O_2, and N_2 self-consistently including the large-scale transport and mutual diffusion in both the vertical and the horizontal. As in GFS, ozone, water vapor, and cloud water are also transported. The simplified stratospheric ozone photochemistry, as described in McCormack et al. (2006), is implemented in both WAM and GFS. Additional physical processes incorporated in the extended model domain include UV and EUV radiative heating, infrared radiative cooling with the breakdown of local thermodynamic equilibrium, nonorographic gravity waves, ion drag, and Joule heating. The current version of WAM uses a spectral resolution T62, corresponding to a horizontal resolution of ~200 km in latitude-longitude. The high-latitude electrical potential is provided by the Weimer model (Weimer, 1995). The ionosphere in the standalone version of WAM is specified by the empirical model of Chiu (1975). WAM has been extensively validated and described in the literature over the last decade (Akmaev, 2011; Akmaev et al., 2008, 2009, 2010; Akmaev & Juang, 2008; Fuller-Rowell, Akmaev, et al., 2008), in particular in regard to simulations of generic and specific sudden stratospheric warmings and their effects on the ionosphere (Fang et al., 2012; Fuller-Rowell et al., 2010, 2011; Wang et al., 2011).

To reproduce the day-to-day and seasonal thermospheric variability, several key physical parameterizations were recently introduced in WAM: (1) The solar heating in WAM is calculated using updated parameterization described in Solomon and Qian (2005). (2) The auroral ionization is defined by an empirical model based on TIROS-NOAA satellite data (Fuller-Rowell & Evans, 1987). (3) To simulate seasonal variations of the mean flow and tidal amplitudes in the mesosphere and lower thermosphere, the nonstationary gravity wave physics were implemented in WAM in addition to the orographic gravity wave drag scheme originally from the GFS. The variant of the linear saturation scheme of Lindzen (1981) with the background wave dissipation due to molecular viscosity and heat conductivity was adapted to describe the momentum and energy deposition along with the eddy mixing (viscosity and heat conduction) induced by gravity wave instability.

The nonstationary waves with the horizontal phase velocities from 5 to 60 m/s were launched in four main azimuths in the troposphere (500 hPa) with the horizontal wavelength of 150 km. The specification of the vertical momentum flux of gravity waves at the launch level with intermittency (efficiency) factor of 0.1 was tuned to reproduce the seasonal variations of the zonal mean flow (zonal winds) in the mesosphere and lower thermosphere as suggested by the Upper Atmosphere Research Satellite (UARS) (1991–1997) zonal wind climatology (Swinbank & Ortland, 2003).

The GIP is an upgraded version of the ionosphere-plasmasphere component of the Coupled Thermosphere Ionosphere Plasmasphere model with Electrodynamics (CTIPe). It solves coupled equations of continuity, momentum, and energy balance equations along the magnetic field lines and calculates time-dependent ionospheric and plasmaspheric densities, temperatures, and velocities on a global, three-dimensional grid (Fang et al., 2009). It consists of a low- and middle-latitude region where interhemispheric transport along closed flux tubes is taken into account, and a high-latitude portion, where plasma can flow across the upper boundary of 10,000 km, which depends on latitude. The horizontal resolution in the low-latitude region is about 1° in latitude and 4.5° in longitude. In altitude, it covers the plasmasphere and provides information from 100 km to higher than 20,000 km. For the magnetic coordinates, instead of the tilted dipole structure, GIP utilizes a Magnetic Apex coordinate system (Richmond, 1995) in which a global three-dimensional grid of magnetic field lines is created by tracing through the full International Geomagnetic Reference Field. The electric fields at low and middle latitudes are calculated by the electrodynamic solver (Richmond, 1995) using the field line-integrated conductivities from GIP and neutral winds from WAM. The same electric field is also used for the plasma transports in GIP. The solar ionization used in GIP is consistent with the solar parameterization used in WAM. The nighttime ionization rates used in the model are spatially uniform and have been described in Richmond and Maute (2013). The modular construction allows for GIP to be easily coupled to any kind of background neutral atmospheric models.

In this study, the variability in the ionosphere is simulated using the WAM and GIP through a one-way coupled scheme. Hourly thermospheric parameters including neutral winds (zonal, meridional, and vertical wind), neutral temperature, and neutral density (O, O_2, and N_2) simulated by WAM are used to drive the GIP. The vertical wind is calculated using WAM outputs through considering rate of change of the height of a pressure level, divergence of horizontal wind, and advection of the height of the pressure levels (Fuller-Rowell, 2014). Since the Joule heating rates in WAM are underestimated compared to those calculated in the CTIPe model, Joule heating rates are doubled in all WAM simulations in this study. Simulations are carried out for a 2-month period (June–July) in 2012. The period was chosen because of its strong variations in solar and geomagnetic activities, which help us to mimic a longer period that covers various levels of solar and geomagnetic activity. Figure 1 shows the 10.7-cm solar radio flux ($F_{10.7}$), K_p index, B_z component of interplanetary magnetic field, and hemispheric power (GW) used to drive the NOAA/TIROS empirical model for the auroral pattern (Fuller-Rowell & Evans, 1987) during June–July 2012. The hemispheric power was based on particle precipitation fluxes and energies measured from NOAA's Polar Orbiting Environmental Satellites (POES), which is archived in NOAA/SWPC database. A good range of solar activity levels with a few moderate geomagnetic storms can be found in the selected period. Clear 27-day solar rotation is also shown. In the simulation, instead of using $F_{10.7}$, the solar activity at different wavelengths is specified daily by several satellite observations. The solar spectrum parameters in wavelengths between 0.05 and 0.8 nm are from NOAA GOES X-ray Sensor, 0.8 to 7 nm are from NASA TIMED Solar EUV Experiment (SEE), 7 to 105.0 nm are from NASA SDO EUV Variability Experiment (EVE), and 105.0 to 170 nm are again from TIMED SEE. The geomagnetic activities are driven by the 5-min IMF/solar wind parameters. Since the daily solar spectrum is calculated, any short-term or flare effects would not be captured in our simulation. The aurora ionization is parameterized by NOAA-TIROS with 5-min resolution during the period. The lower atmospheric perturbations are internally generated by WAM physics through the tides and waves from the lower atmosphere.

Three simulations are performed to quantify the relative contribution of the sources driving the variability: (1) WAM-GIP driven by variability including the perturbations from the lower atmosphere and time-varying solar and geomagnetic drivers (referred to as *All Variability Run* in this paper); (2) WAM-GIP driven by variability from the lower atmospheric perturbations and time-varying solar driver; the geomagnetic activity is fixed to the averaged value during the period (referred to as *Lower Atmosphere/Solar Variability Run* in this paper); and (3) WAM-GIP driven by only variability from the lower atmospheric perturbations; the solar and geomagnetic activities are fixed to the averaged values during the period (referred to as *Lower Atmosphere Variability Run* in this paper).

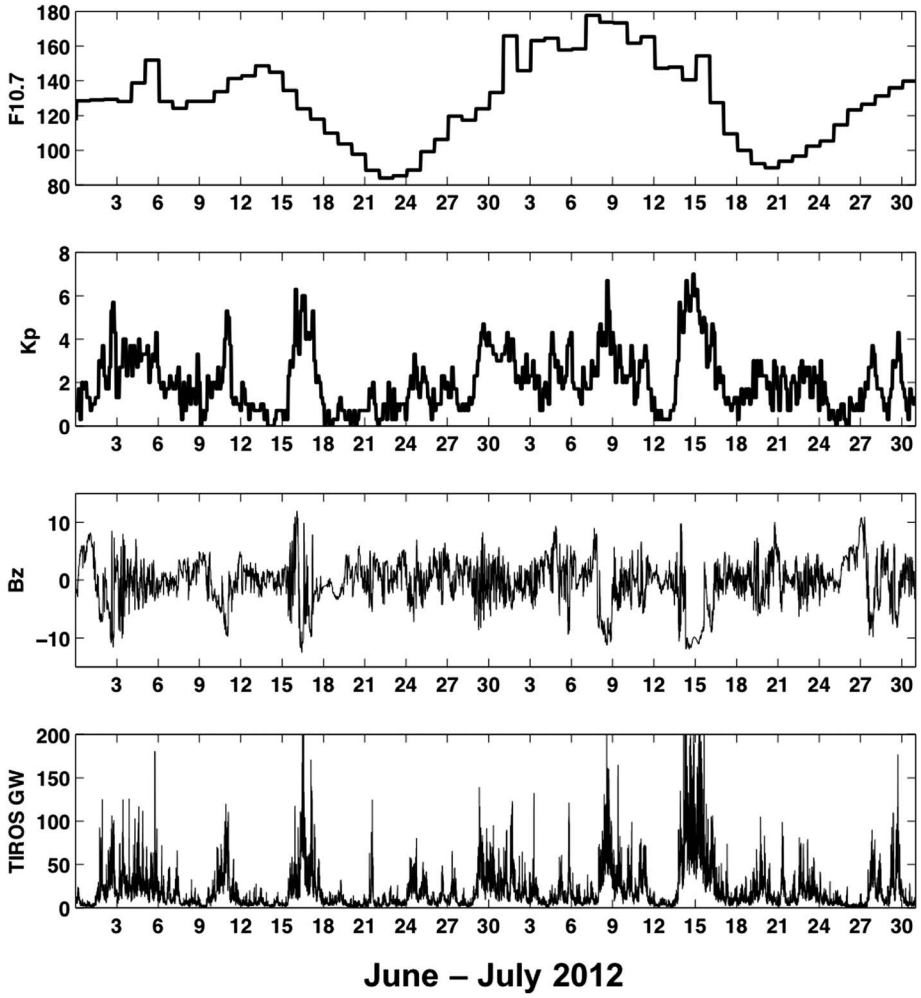

Figure 1. The $F_{10.7}$ cm solar flux, 3-hr geomagnetic activity index K_p, 5-min interplanetary magnetic field (IMF) *Bz* component, and 1-min hemispheric power used in TIROS/NOAA statistical model during June–July 2012.

3. Results and Discussion

Figure 2 illustrates the day-to-day variability of thermospheric parameters (O to N_2 ratio, neutral temperature, zonal wind, and meridional wind) as a function of latitude at 0° longitude at 300-km altitude simulated by WAM. The climatology of these simulated parameters shows expected hemispheric differences for June solstice. Comparing results from the All Variability Run (left) and Lower Atmosphere Variability Run (right) shows that the changes of these thermospheric parameters are strongly controlled by solar and geomagnetic activities. For example, thermospheric temperature around 22 June was much lower than other days, which corresponds to the very low solar activity and very quiet geomagnetic conditions shown in Figure 1. Between 15 and 18 July, the enhancement of global thermospheric temperature is caused by a strong geomagnetic storm that occurred on 15 July. During the storm period, the magnitudes of zonal and meridional neutral winds also strengthen and extend to much lower latitudes. These day-to-day changes in thermospheric parameters from the lower atmosphere variability run can be observed but are much less pronounced.

Figure 3 shows the amplitudes of two thermospheric tidal modes calculated from the zonal wind at 115 km, the migrating semidiurnal westward propagating tide with zonal wave number 2 (SW2), and the eastward propagating nonmigrating diurnal tide with zonal wave number 3 (DE3), during the June period from the All Variability Run (left) and Lower Atmosphere Variability Run (right). Previous studies have shown that the amplitude and phase of the SW2 strongly dominate the variability of daytime equatorial electric field at the low-latitude ionosphere (e.g., Fang et al., 2013; Millward et al., 2001), while the DE3 tide also

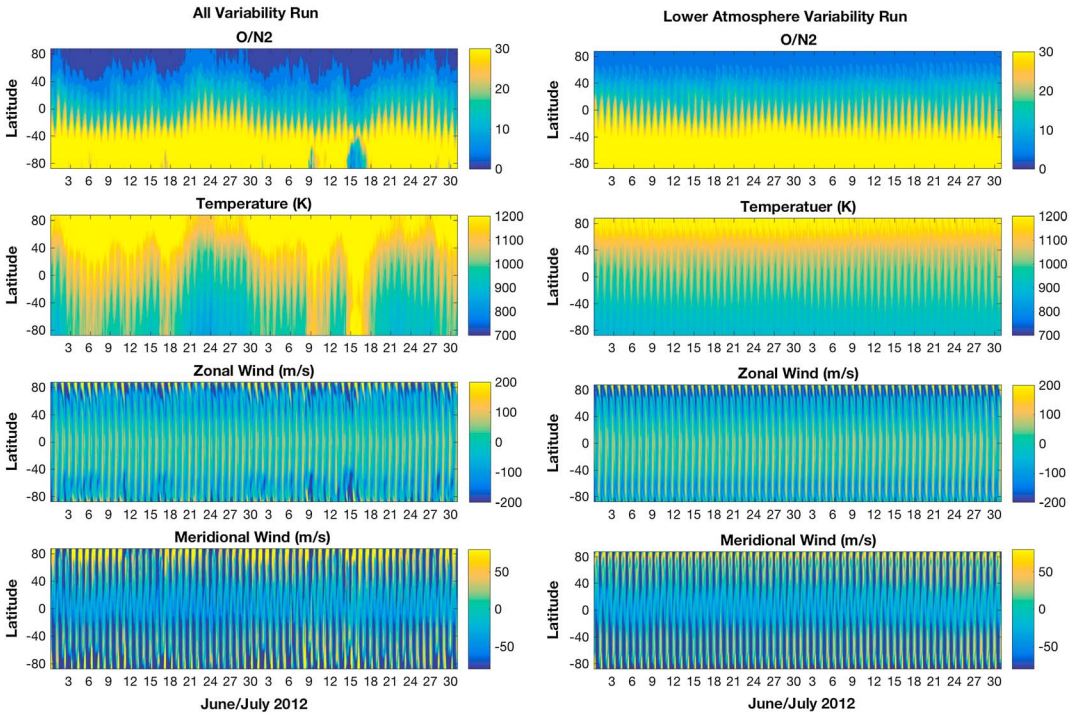

Figure 2. Thermospheric parameters (O/N_2, temperature, zonal wind, and meridional wind) at 0° longitude and 300 km simulated from (left) All Variability Run and (right) Lower Atmosphere Variability Run during June–July 2012.

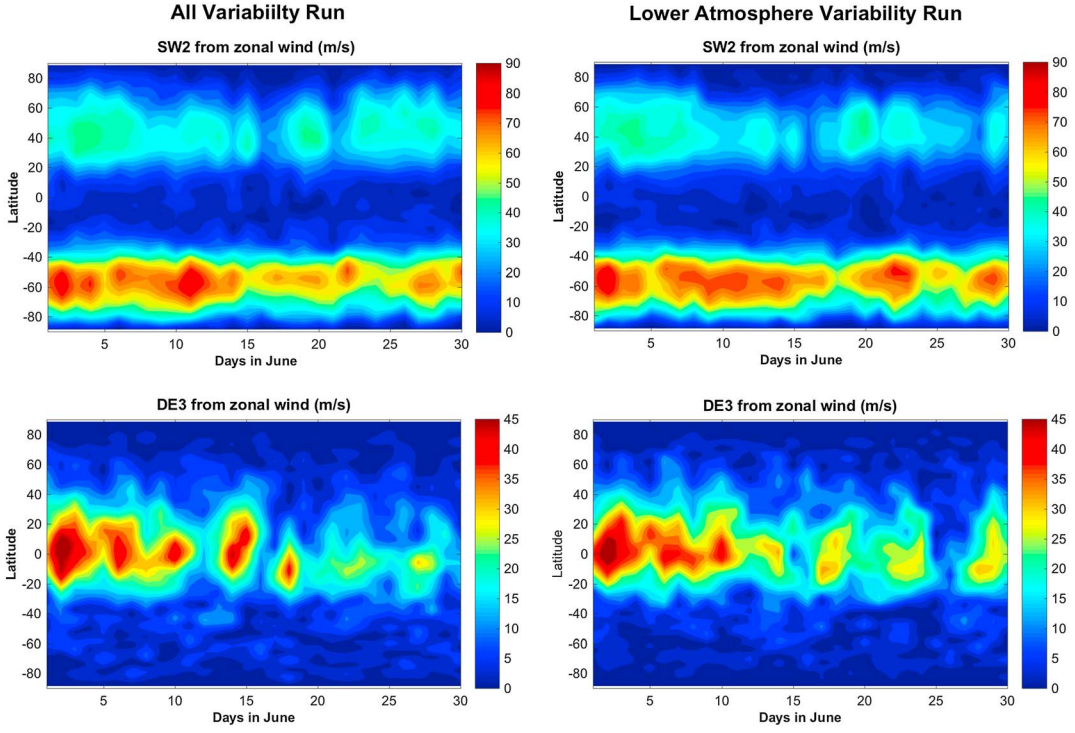

Figure 3. Amplitudes of thermospheric tides SW2 and DE3 calculated from the zonal wind at 115 km from (left) All Variability Run and (right) Lower Atmosphere Variability Run in June–July 2012.

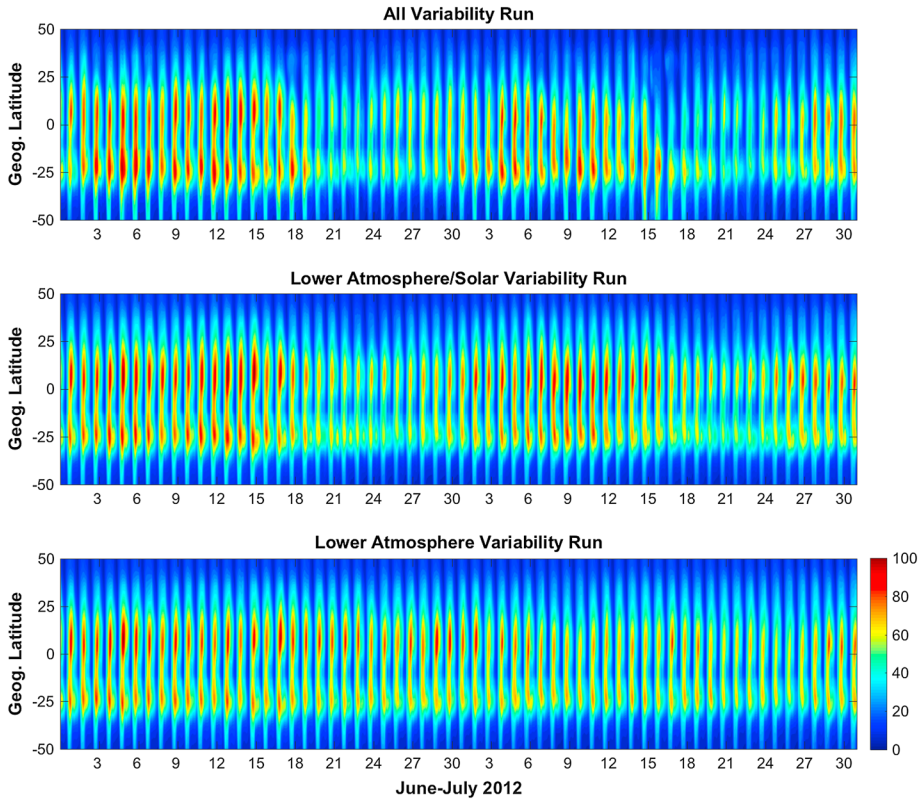

Figure 4. Time variation of TEC at 70°W during June–July 2012 calculated from the (top) All Variability Run, (middle) Lower Atmosphere/Solar Variability Run, and (bottom) Lower Atmosphere Variability Run.

influences the ionosphere through electrodynamic processes and leads to strong longitudinal variations in both daytime and nighttime ionospheric densities at the low-latitude region (e.g., Fang et al., 2009; Immel et al., 2006). Our simulation shows that amplitude of SW2 peaks at around 60°S and the DE3 peaks near the geographic equator, which are consistent with previous studies (e.g., Akmaev et al., 2008). Day-to-day variations of these tidal amplitudes can clearly be seen in both cases. Comparing these two cases, the maximum amplitudes of these tides do not show dramatic differences with solar and geomagnetic activity variations included, indicating that lower atmosphere forcing is the dominant source of variability in the lower thermosphere. Note that the lower thermosphere, where these tides are significant, is also the altitude driving significant dayside electrodynamics. This comparison demonstrates the similarity of contributions from the lower atmospheric perturbation to the upper atmosphere despite the differences in their solar and geomagnetic conditions. This also gives us confidence when interpreting the results for the simulations separating the lower atmospheric perturbations from the impact of solar and geomagnetic activity on the ionosphere.

Variability in the TEC and *F* region N_mF_2 from lower atmosphere forcing can arise either from direct propagation of waves to the upper thermosphere or through changes in *E* region dynamo wind and the electrodynamic connection to the *F* region. Also note that the electrodynamics is a global response, so variation in the dayside drivers of tidal wind and conductivity can also change nightside electrodynamics. The *F* region dynamo on both the day and nightside will add to the dayside *E* region variability.

Figure 4 shows the simulated TEC at 70°W during June–July 2012 from the All Variability Run (top), Lower Atmosphere/Solar Variability Run (middle), and Lower Atmosphere Variability Run (bottom). The magnitudes of simulated TEC from the All Variability Run are compared reasonably well with GPS-TEC observed by the Low-Latitude Ionosphere Sensor Network during the same period in 2012 in the South American sector located near longitude 70°W, which was shown in Figure 1 of Khadka et al. (2018). The comparison also demonstrates that the magnitude of the variability is reasonably consistent with the observations, with

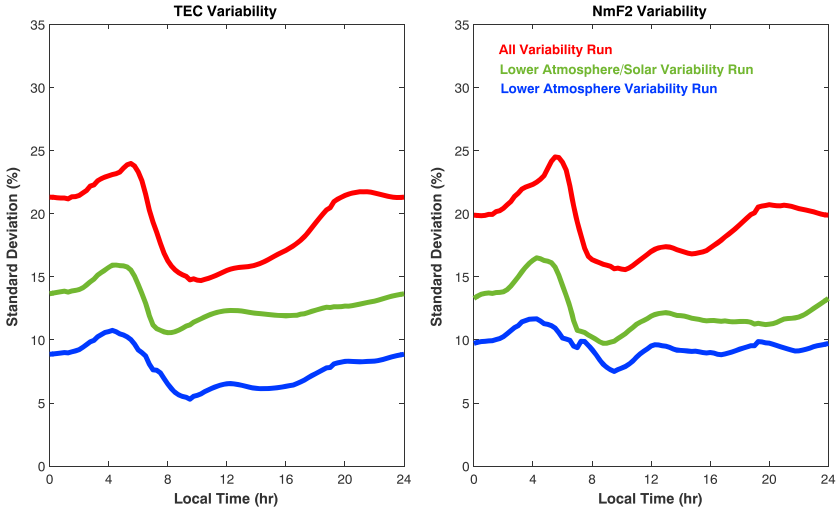

Figure 5. Local time variation of ionospheric relative variability (i.e., percentage of standard deviation) in (left) TEC and (right) N_mF_2 calculated from the 13 stations used in Rishbeth and Mendillo (2001). Results of All Variability Run (red), Lower Atmosphere/Solar Variability Run (green), and Lower Atmosphere Variability Run (blue) are shown.

strong day-to-day variability in TEC and with similar latitudinal distribution. Results from the top two panels of Figure 4 demonstrate that ionospheric density variation is strongly associated with changes in solar activity. The electron density at the equatorial ionization anomaly (EIA) region is significantly larger when the solar activity is higher (see Figure 1). Impact of geomagnetic activity can be estimated through comparing the top two panels. When geomagnetic activity is included in the simulation, the asymmetry between north and south crests becomes much larger. In particular, overall smaller density at the northern EIA crest compared to those at southern EIA crest. The asymmetry also becomes more pronounced when geomagnetic activity enhances (i.e., periods during 15–18 June and 14–18 July). The enhancement of hemispheric asymmetry related to the geomagnetic activity has been previously examined using ionosonde observation (Araujo-Pradere et al., 2004). Their study suggests that the thermospheric circulation cells due to energy input related to geomagnetic storms could enhance the mean molecular mass in the summer hemisphere and reduce the mean molecular mass in the winter hemisphere at the middle and low latitudes. The enhanced and reduced mean molecular mass then further leads to the negative and positive ionospheric responses, respectively. The changes of the boundary between regions of increased and decreased composition also cause the increasing variability in winter midlatitudes. Their study provides a good observational evidence and an explanation of our simulation results when geomagnetic activity is included. The bottom panel demonstrates the ionospheric density from the run with fixed solar and geomagnetic activities, which still shows clear day-to-day variation. Comparing the rather small day-to-day variability in thermospheric parameters at 300 km (right side in Figure 2) and strong day-to-day changes in tidal amplitudes (right side in Figure 3), it shows that the day-to-day ionospheric variability from this run is clearly related to the changes in the dynamo electric fields resulting from different thermospheric tides and other waves from the lower atmosphere.

In the study of Rishbeth and Mendillo (2001), N_mF_2 data from 13 stations (see Table 3 in Rishbeth and Mendillo) are selected for the long-term ionospheric variability study. The selected stations are mainly located at middle and high latitudes. In their study, the relative variability is expressed as the absolute standard deviation of $N_mF_2(\sigma\ (N_mF_2))$ as a percentage of mean value of N_mF_2. Selecting the same locations as these 13 stations and carrying out the same percentage calculation used in Rishbeth and Mendillo, relative variability of ionospheric TEC and N_mF_2 at different local times are calculated from the three 2-month simulation runs and shown in Figure 5. Overall, the relative TEC and N_mF_2 variability shows similar magnitude when all the drivers are included. Their variabilities are generally larger during the nighttime than in the daytime. The largest and smallest variability is found to occur at around the dawn period (~6 LT) and the morning period (~10 LT), respectively. Simulations including all sources of variability show that both TEC and N_mF_2 relative variabilities range between 15% and 20% in the daytime and between 20% and 25% at night. These values

Table 1
The Contributions of Lower Atmosphere, Solar Activity, and Geomagnetic Activity to Relative TEC and N_mF_2 Variability for Daytime (7–18 LT), Nighttime (18–7 LT), and Whole-Day Mean, Calculated From Figure 6

Relative variability (%)	TEC			N_mF_2		
	Day	Night	Mean	Day	Night	Mean
Lower atmosphere	6.3	9	7.8	8.9	10.1	9.6
Solar activity	9.9	10.5	10.2	6.7	8.6	7.7
Geomagnetic activity	11.2	16.8	14.2	12.8	16.2	14.6
Total	16.2	21.8	19.1	17	21	19.1

Note. See text for more details.

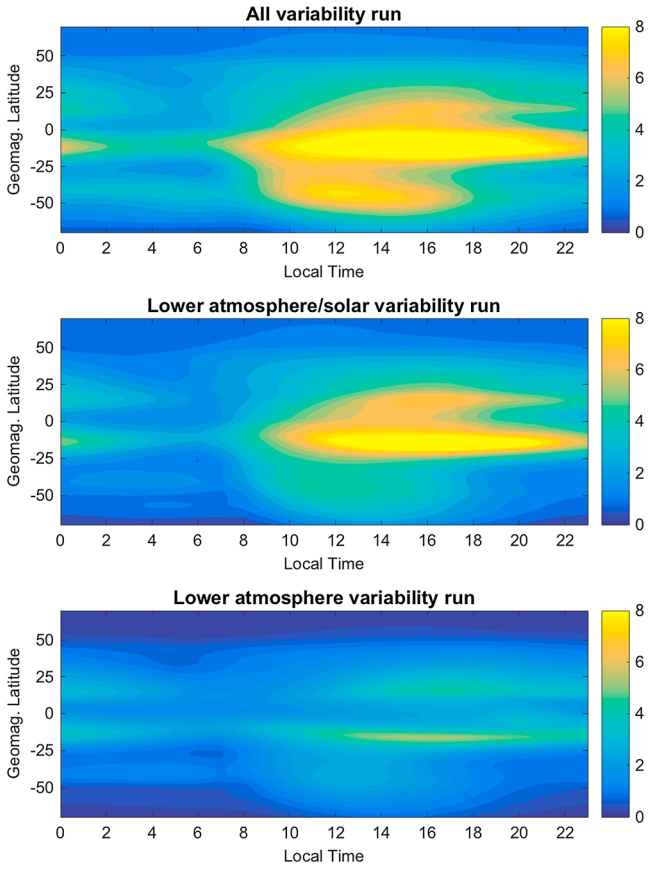

Figure 6. Local time variation of absolute TEC variability during the 2-month period, organized by magnetic latitude and averaged over all longitudes for (top) All Variability Run, (middle) Lower Atmosphere/Solar Variability Run, and (bottom) Lower Atmosphere Variability Run.

are comparable but smaller than the results from Rishbeth and Mendillo (20% by day and 33% by night under medium solar activity), which could be due to the shorter sampling period in our simulation (northern summer only) and the north/south difference in the distribution of the stations. Comparing our results of Lower Atmosphere Variability Run (blue lines in Figure 5) to previous WAM-GIP simulations in Fang et al. (2013), our latest simulation seems to capture less variability. However, the discrepancy between these results is mainly caused by the selection of the locations. Ionospheric variability calculated from the 13 locations is used in this study, while the variability from a particular longitude and latitude was shown in Fang et al. (2013). The day-to-day variability of the ionosphere tends to be larger at lower latitudes due to the direct impact of electrodynamics, solar radiation, and transport related to the transequator wind. The 13 stations used in Rishbeth and Mendillo are mostly located at middle and high latitudes (only three stations located below magnetic latitude 35°). Results of averaged ionospheric variability from the selected 13 stations are expected to be smaller compared to those from stations located at lower magnetic latitude regions.

Figure 5 also demonstrates that the diurnal variations in TEC and N_mF_2 from the All Variability Run are slightly different, with larger variability in TEC in the night and a daytime peak at 13 LT in N_mF_2. This result suggests that the variability from different ionospheric measurements at different local times may lead to different conclusions. Ionospheric variability observed by satellites at different orbits may also reflect variability associated with different physical processes. To further understand the contribution of different drivers to ionospheric variability, the differences of relative TEC and N_mF_2 variability and the contributions of different sources are calculated. To estimate the relative contribution of variability from the three sources, they are assumed to be decorrelated, so that the total variability is the square root of sum of squares of total variability from each source term.

$$(Total\ variablity)^2 = (Lower\quad atmosphere\ varibility)^2 + (Geomagnetic\ variability)^2 + (Solar\ variability)^2$$

The values from Figure 5 can then be used to quantify the variability from each source separately. For example, the values for lower atmosphere variability are obtained directly from the blue lines (Lower Atmosphere Variability Run), those for the geomagnetic variability are derived from the square root of difference between square of All Variability Run and square of Lower Atmosphere/Solar Variability Run (i.e., $\sqrt{(\text{red line})^2 - (\text{green line})^2}$), and values for the solar variability can be further calculated once the values of other two sources are identified. The contribution of each source is listed in Table 1. The results are further averaged over the daytime (7–18 LT), nighttime (18–7 LT), and all local times. The assumption that the signals are not correlated may not be valid given the complexity of dynamic and electrodynamic processes in the ionosphere-thermosphere system and considering the unknown nonlinear effect among these drivers.

Results in Table 1 show that for both TEC and N_mF_2 geomagnetic perturbations are the main source of the ionospheric relative variability during both daytime and nighttime. The contribution of geomagnetic activity is also larger during the nighttime than in the daytime. The strong impact of geomagnetic activity variability on the TEC and N_mF_2 reflects the sensitivity of ionosphere in responding to global dynamics associated with geomagnetic activity. Besides geomagnetic activity, relative TEC

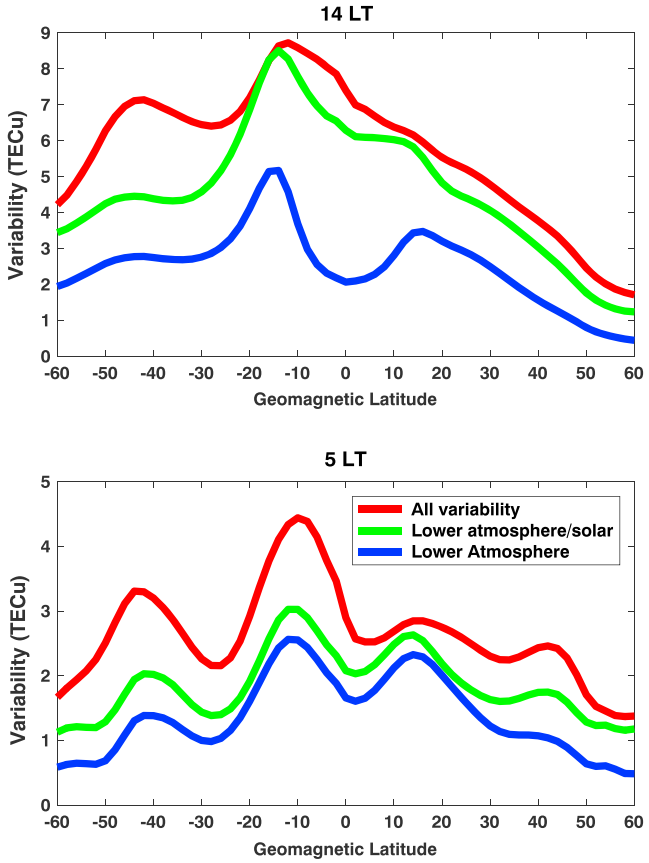

Figure 7. Latitudinal distribution of absolute TEC variability at 5 and 14 LT extracted from Figure 6. Results for All Variability Run (red lines), Lower Atmosphere/Solar Variability Run (green lines), and Lower Atmosphere Variability Run (blue lines) are shown.

variability is mostly contributed by solar activity variation, while relative N_mF_2 variability is mostly associated with the lower atmosphere perturbations. The daytime ionosphere is largely produced by the solar X-ray and EUV. At night, ionospheric *F* region density still remains, which is resulted from the residual dayside density and the starlight or the solar radiation scattered through the geocoronal. Several important photoionization sources for the maintenance of nighttime ionosphere, such as Lyman-α (1216 Å), Lyman-β (1026 Å), He I (584 Å), and He II (304 Å), are considered in our simulation for the nighttime ionization. Our results suggest that the photoionization plays a much more important role in controlling the overall variability in the integrated quantity (i.e., TEC) than a localized quantity (i.e., N_mF_2). The impact of lower atmosphere, which is largely through the electrodynamic processes, has stronger and more direct control in the *F* region height and density. Our results, which show that the dominated sources of relative N_mF_2 variability at these 13 locations are from the lower atmosphere perturbation and geomagnetic activity, also support the conclusions made in Rishbeth and Mendillo (2001).

The relative variability shown in Figure 5 and Table 1 is calculated by taking percentage of values after dividing the standard deviation of TEC and N_mF_2 from their mean values at each local time and location. At early morning (4–6 LT), the ionospheric density tends to be very low at all locations, which leads to a very low background mean. Thus, the percentage variability would mostly show larger values at these local times (see Figure 5). To better quantify the root causes of variability at different local times and locations, in the following part of our paper the standard deviation calculated from our simulations is shown as *absolute variability* without calculating the percentage. We also mainly focus on explaining the sources of absolute variability in ionospheric TEC.

Since the ionospheric morphology largely depends on local time and is strongly controlled by the geomagnetic coordinate, we rearrange the TEC values according to their local time, organized with respect to magnetic latitude, and average the variabilit from all longitudes. The standard deviation (i.e., the absolute TEC variability) is then calculated at each local time and magnetic latitude. The distributions of absolute TEC variability as a function of magnetic latitude and local time from three different runs are shown in Figure 6. For all three cases, the absolute variability shows that stronger magnitudes at lower latitudes throughout all local times and are much larger during the daytime than in the nighttime. Comparing results from these three runs, it shows that with geomagnetic activities included in the simulation the hemispheric asymmetry of the variability becomes much larger. Subtracting results of the All Variability Run by the Lower Atmosphere/Solar Variability Run, an additional enhanced variability appears at middle latitudes in the Southern Hemisphere (winter hemisphere). The peak magnitude from the All Variability Run is ~9.8 TECu (10^{16} el/m^2) and located at 14°S in magnetic latitude at 16 LT.

To further investigate the variability in different cases, latitudinal profiles of variability at 14 LT (top) and 5 LT (bottom) of different cases are shown in Figure 7. At the low-latitude region, the variability clearly shows larger magnitudes in the Southern Hemisphere at both local times. The hemispheric asymmetry is associated with the transequatorial wind from the summer (north) hemisphere to the winter (south) hemisphere. Also, at both local times, much stronger variability shows at midlatitudes in the Southern Hemisphere from the all variability run. The differences between All Variability Run and two other cases can be attributed to the impact of geomagnetic activity on the thermosphere-ionosphere system. Several days of higher geomagnetic activities did occur during our study period. When geomagnetic activity increases, the solar wind energy crossing the magnetopause leads to joule heating in the high-latitude ionosphere-thermosphere system and results in overall thermosphere temperature increases at high

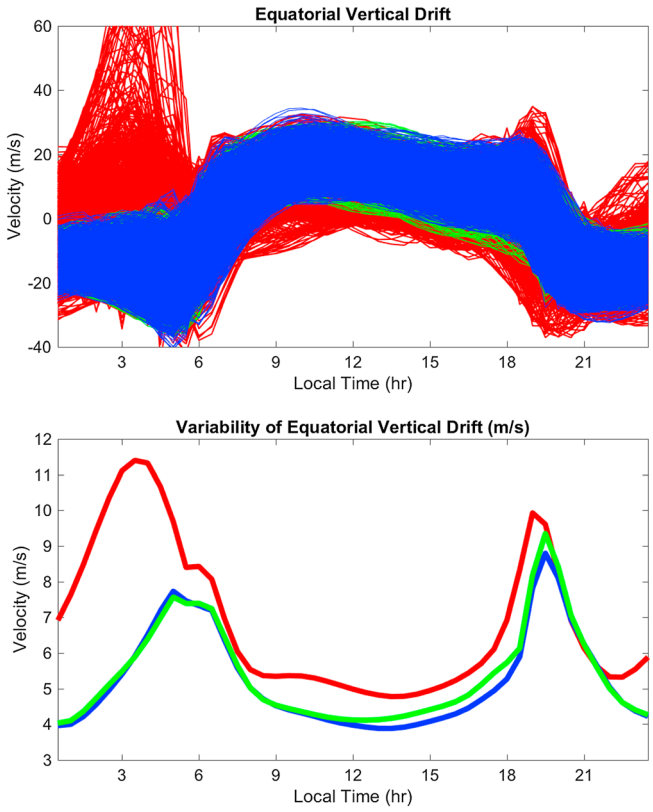

Figure 8. (top) Diurnal variation of equatorial vertical drifts calculated at all longitudes from All Variability Run (red), Lower Atmosphere/Solar Variability Run (green), and Lower Atmosphere Variability (blue). (bottom) Local time variation of the drift variability (i.e., standard deviation) for different simulation runs.

latitudes. The increased temperature further modulates the global thermospheric composition and wind circulation. Changes in neutral composition directly impact the ionospheric density through the recombination processes, while changes in neutral wind has influences in the low-latitude ionospheric density through electrodynamic processes and in midlatitudes ionosphere through the enhanced equatorward wind that pushes plasma to higher altitudes along the flux tubes. Our study suggests that the variability of geomagnetic activity leads to a larger variability at the midlatitude ionosphere especially in the winter hemisphere where the averaged ionospheric density tends to be smaller. Similar result has been demonstrated using observations in Araujo-Pradere et al. (2004) and is believed to be associated with the changes of the thermospheric composition during geomagnetic storms. More global observations of thermospheric composition from satellite measurement in the future may help to provide a definite answer to the phenomenon.

Figure 7 also shows that the impact of geomagnetic activity is stronger in the nighttime than in the daytime at low latitudes (see the differences between red and green lines at the two local times). To understand what parameter contributes to the variability of the low-latitude ionosphere, Figure 8 shows equatorial vertical drifts at the magnetic equator from all longitudes and all three cases of simulations (top) and the standard deviations of these drifts (bottom). The equatorial vertical drifts from the Lower Atmosphere Variability Run (blue lines) demonstrate significant variability throughout all local times. However, the range of variability from this run is similar to those from the Lower Atmosphere/Solar Variability Run (green lines), which suggests that the variability of equatorial vertical drift is dominated by the lower atmosphere perturbation in these two cases. Time-varying solar radiation during this period does not contribute extra variability to the drifts. The results agree with results from Scherliess and Fejer (1999) showing that the magnitudes of daytime drifts are less

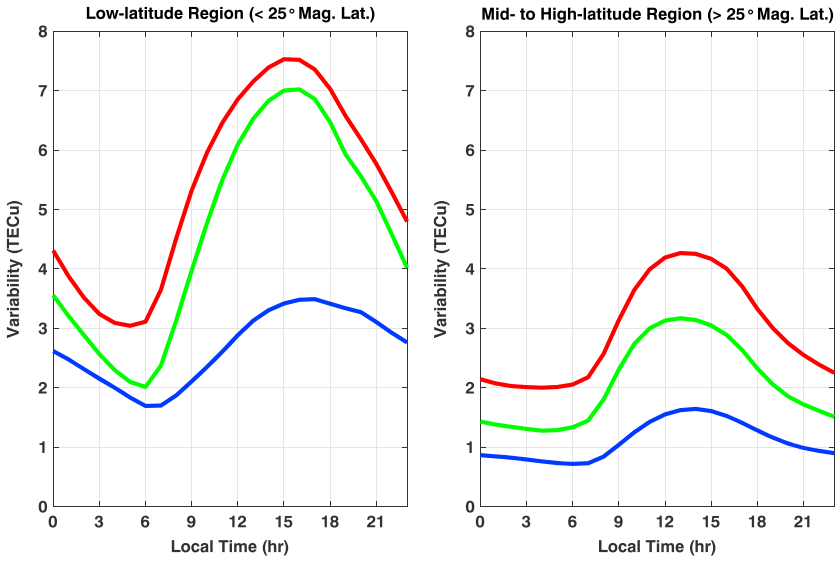

Figure 9. Local time variation of absolute TEC variability averaged over the low-latitude region and the middle- to high-latitude region. Results of All Variability Run (red lines), Lower Atmosphere/Solar Variability Run (green lines), and Lower Atmosphere Variability Run (blue lines) are shown.

Table 2
The Contributions to Absolute TEC Variability at Different Latitude Regions From Lower Atmosphere, Solar Activity, and Geomagnetic Activity During Daytime, Nighttime, and All Local Times

Absolute variability (TECu)	Low latitude			Middle-high latitude		
	Day	Night	Mean	Day	Night	Mean
Lower atmosphere	2.8	2.5	2.6	1.3	0.9	1.1
Solar activity	4.8	2.6	3.7	2.3	1.2	1.7
Geomagnetic activity	3	2.4	2.7	2.4	1.7	2.1
Total	6.3	4.3	5.3	3.6	2.3	2.9

sensitive to the solar activity. The drift results indicate that the differences between the Lower Atmosphere/Solar variability Run (green lines) and Lower Atmosphere Variability Run (blue lines) at low latitudes shown in Figure 7 are not caused by the equatorial drift but by the difference of ionization level caused by solar ionization. This also explains why the differences are much larger in the daytime than in the nighttime.

The equatorial vertical drifts from the All Variability Run (red lines in Figure 8) show larger variability than the two other cases and the range of variability becomes very large during the postmidnight period. The magnitudes of these large vertical drifts can reach 60–80 m/s and generally happen on days when strong geomagnetic activity is present. The large upward drifts are largely associated with the thermospheric winds that are modulated by the geomagnetic storm. During geomagnetic storms, the propagation of high-speed gravity waves launched by auroral heating can reach midlatitude in an hour and can reach the equator and penetrate into the opposite hemisphere within 3 hr (Fuller-Rowell et al., 2008). Large-scale gravity waves provide the mechanism for transmitting changes in pressure gradients around the globe. Within a few hours of onset time of geomagnetic storms, the peak wind responses at auroral latitude would be close to 700 m/s, while at middle and low latitudes the wind surges could be about 100–150 m/s above the background circulation. The enhanced equatorward wind caused by high-latitude heating and the Coriolis force constitute strong westward wind at midlatitude (Blanc & Richmond, 1980). The westward wind (i.e., disturbance dynamo) further leads to a reverse *Sq* current vortex, therefore reducing or even reversing the eastward electric field on the dayside and reducing or reversing the normal westward electric field on the nightside (Maruyama et al., 2005). Comparing the standard deviations of drifts from the three cases, larger variability can be found at 5 and 20 LT in all cases. The variability of equatorial vertical drift from the all variability run is overall stronger than the two other cases, and the differences are much larger in the nighttime than in the daytime. The variability in the equatorial vertical drift has direct impact on the distribution of ionospheric density and recombination process depending on their heights in both the daytime and nighttime. This partly explains the larger variability of TEC from the all variability run compared to other two cases at 5 LT at low latitudes (see Figure 7).

To better understand the local time behavior of ionospheric variability at different latitudinal sectors, the variabilities in both hemispheres shown in Figure 7 are further averaged and divided into the low-latitude region (less than 25° geomagnetic latitude) and the middle- to high-latitude region (higher than 25° geomagnetic latitude) at each local time. The regional averaged results from there different runs are shown in Figure 9. In general, the variability is much larger at low latitudes. Carrying out the same calculations for Table 1, the contributions of lower atmosphere, solar activity, and geomagnetic activity at the different latitude regions are shown in Table 2. The numbers in Table 2 suggest that at the low-latitude region the main contributor for ionospheric variability is the solar variation and the contribution is much larger in the daytime than at night. Lower atmosphere perturbation contributes almost equally with geomagnetic perturbations throughout the day. At middle and high latitudes, during the daytime the contributions from solar activity and geomagnetic activity are compatible, while at night the geomagnetic activity is the main contributor. Lower atmosphere perturbation at this region is not as important as those at low latitudes.

4. Conclusions

Our simulation using WAM-GIP demonstrates a significant amount of ionospheric day-to-day variability. The variability shows pronounced longitudinal, latitudinal, and local time dependencies. Our results suggest that the geomagnetic perturbations are the most important contributor to the relative variability of ionospheric TEC and N_mF_2, while the solar activity and lower atmosphere perturbations contribute differently for N_mF_2 and TEC. Several key findings are summarized below.

1. Averaging over 13 locations that are mostly located in middle and high latitudes, our results show that relative N_mF_2 variability is largely driven by geomagnetic activity followed by lower atmospheric perturbation, then solar activity. Relative TEC variability is largely driven by the geomagnetic followed by solar activity, then lower atmosphere perturbation.

2. Averaging the variability over all longitudes and organizing them with geomagnetic latitude show that absolute value in TEC variability at low latitudes is largely controlled by solar activity. For middle and high latitudes, solar and geomagnetic activities contribute roughly equally to the absolute TEC variability.
3. The variability of equatorial vertical drift is largely driven by lower atmosphere forcing during the daytime. At nighttime, especially during the postmidnight period, the drift is strongly influenced by geomagnetic activity.
4. Simulation results indicate that larger ionospheric variability can be found at the low-latitude region, particularly in the winter hemisphere. Also, geomagnetic activity is responsible for the large TEC variability at midlatitude in the winter hemisphere during the daytime period.

Our simulation successfully reproduces the majority of ionospheric variability using the state-of-the-art WAM-GIP models under quiet-to-moderate solar and geomagnetic conditions, which incorporate changes from solar and geomagnetic activity and the metrological impact on the upper atmosphere and ionosphere. However, comparing our results with the long-term study by Rishbeth and Mendillo (2001), the day-to-day variability from our simulation is about 5%–10% smaller. The smaller variability shows that our simulation may be related to the underestimation of Joule heating in the thermosphere, since the small-scale electric field variability is not currently considered in WAM-GIP (Codrescu et al., 2008). The simulation is carried out with a one-way coupled scheme. More realistic variability may be simulated with the two-way coupled models. Carrying out simulations using the WAM Data Assimilation System (Wang et al., 2011), which incorporates the realistic lower atmosphere weather, may also help to capture much more realistic thermospheric weather. Simulation with a much longer time period will also need to be carried out to investigate season/latitude variations and to better validate simulation results against the observations.

Our study has suggested that ionospheric variability strongly depends on local time, latitudes, and altitudes. Variability calculated from long-term ground-based measurements at different locations may result in very different conclusions. With different physics dominating different regions of the ionosphere, variability measured by satellites at different orbits might also result in different conclusions. This simulation study presents the first numerical simulation that intends to quantify different sources of ionospheric variability. The development of WAM has provided us a valuable capability to diagnose the complex coupled system. WAM is currently being transitioned into operation at NOAA SWPC. Results from this study set an important paradigm for the whole atmosphere modeling community, and the knowledge gained from this study will be extremely useful for improving the operational model in order to provide accurate information to the I-T community, and SWPC customers in the near future.

Acknowledgments
The authors acknowledge support from the NASA Heliophyscis Grand Challenges Research grant NNX14AI17G and NSF CEDAR Program award number 1243129 for this research. Computational resources were provided by the NOAA R&D high performance computing system and NOAA/SWPC. Simulation outputs in ASCII are archived in NOAA National Weather Service (NWS) computer system and are also available through open access (https://doi.org/10.5281/zenodo.1409821).

References

Akmaev, R. A. (2011). Whole atmosphere modeling: Connecting terrestrial and space weather. *Reviews of Geophysics*, *49*, RG4004. https://doi.org/10.1029/2011RG000364

Akmaev, R. A., Fuller-Rowell, T. J., Wu, F., Forbes, J. M., Zhang, X., Anghel, A. F., et al. (2008). Tidal variability in the lower thermosphere: Comparison of Whole Atmosphere Model (WAM) simulations with observations from TIMED. *Geophysical Research Letters*, *35*, L03810. https://doi.org/10.1029/2007GL032584

Akmaev, R. A., & Juang, H.-M. H. (2008). Using enthalpy as a prognostic variable in atmospheric modeling with variable composition. *Quarterly Journal of the Royal Meteorological Society*, *134*(637), 2193–2197. https://doi.org/10.1002/qj.345

Akmaev, R. A., Wu, F., Fuller-Rowell, T. J., & Wang, H. (2009). Midnight temperature maximum (MTM) in Whole Atmosphere Model (WAM) simulations. *Geophysical Research Letters*, *36*, L07108. https://doi.org/10.1029/2009GL037759

Akmaev, R. A., Wu, F., Fuller-Rowell, T. J., Wang, H., & Iredell, M. D. (2010). Midnight density and temperature maxima, and thermospheric dynamics in Whole Atmosphere Model simulations. *Journal of Geophysical Research*, *115*, A08326. https://doi.org/10.1029/2010JA015651

Araujo-Pradere, E. A., Fuller-Rowell, T. J., & Bilitza, D. (2004). Ionospheric variability for quiet and perturbed conditions. *Advances in Space Research*, *34*(9), 1914–1921. https://doi.org/10.1016/j.asr.2004.06.007

Araujo-Pradere, E. A., Fuller-Rowell, T. J., Codrescu, M. V., & Bilitza, D. (2005). Characteristics of the ionospheric variability as a function of season, latitude, local time, and geomagnetic activity. *Radio Science*, *40*, RS5009. https://doi.org/10.1029/2004RS003179

Blanc, M., & Richmond, A. (1980). The ionospheric disturbance dynamo. *Journal of Geophysical Research*, *85*, 1669–1686. https://doi.org/10.1029/JA085iA04p01669

Chau, J. L., Fejer, B. G., & Goncharenko, L. P. (2009). Quiet variability of equatorial E B drifts during a sudden stratospheric warming event. *Geophysical Research Letters*, *36*, L05101. https://doi.org/10.1029/2008GL036785

Chiu, Y. T. (1975). An improved phenomenological model of ionospheric density. *Journal of Atmospheric and Terrestrial Physics*, *37*(12), 1563–1570. https://doi.org/10.1016/0021-9169(75)90035-5

Codrescu, M. V., Fuller-Rowell, T. J., Munteanu, V., Minter, C. F., & Millward, G. H. (2008). Validation of the Coupled Thermosphere Ionosphere Plasmasphere Electrodynamics model: CTIPE-Mass Spectrometer Incoherent Scatter temperature comparison. *Space Weather*, *6*, S09005. https://doi.org/10.1029/2007SW000364

Fang, T.-W., Akmaev, R., Fuller-Rowell, T., Wu, F., Maruyama, N., & Millward, G. (2013). Longitudinal and day-to-day variability in the ionosphere from lower atmosphere tidal forcing. *Geophysical Research Letters*, *40*, 2523–2528. https://doi.org/10.1002/grl.50550

Fang, T.-W., Fuller-Rowell, T., Akmaev, R., Wu, F., Wang, H., & Anderson, D. (2012). Longitudinal variation of ionospheric vertical drifts during the 2009 sudden stratospheric warming. *Journal of Geophysical Research*, *117*, A03324. https://doi.org/10.1029/2011JA017348

Fang, T.-W., Kil, H., Millward, G., Richmond, A. D., Liu, J.-Y., & Oh, S.-J. (2009). Causal link of the wave-4 structures in plasma density and vertical plasma drift in the low-latitude ionosphere. *Journal of Geophysical Research*, *114*, A10315. https://doi.org/10.1029/2009JA014460

Fejer, B. G. (2002). Low latitude storm time ionospheric electrodynamics. *Journal of Atmospheric and Solar - Terrestrial Physics*, *64*(12-14), 1401–1408. https://doi.org/10.1016/S1364-6826(02)00103-7

Forbes, J. M., Palo, S. E., & Zhang, X. (2000). Variability of the ionosphere. *Journal of Atmospheric and Solar - Terrestrial Physics*, *62*(8), 685–693. https://doi.org/10.1016/S1364-6826(00)00029-8

Fuller-Rowell, T. (2014). Physical characteristics and modeling of Earth's thermosphere. In J. D. Huba, et al. (Eds.), in *Modeling the ionosphere-thermosphere*, *Geophysical Monograph Series* (Vol. 201, pp. 13–27). Chichester, UK: John Wiley. https://doi.org/10.1002/9781118704417. ch2

Fuller-Rowell, T., Codrescu, M., Moffett, R., & Quegan, S. (1994). Response of the thermosphere and ionosphere to geomagnetic storms. *Journal of Geophysical Research*, *99*, 3893–3914. https://doi.org/10.1029/93JA02015

Fuller-Rowell, T., Richmond, A., & Maruyama, N. (2008). Global modeling of storm-time dynamics and electrodynamics. *American Geophysical Union Geophysical Monograph*, *181*, 187.

Fuller-Rowell, T., Wang, H., Akmaev, R., Wu, F., Fang, T.-W., Iredell, M., & Richmond, A. (2011). Forecasting the dynamic and electrodynamic response to the January 2009 sudden stratospheric warming. *Geophysical Research Letters*, *38*, L13102. https://doi.org/10.1029/2011GL047732

Fuller-Rowell, T., Wu, F., Akmaev, R., Fang, T.-W., & Araujo-Pradere, E. (2010). A whole atmosphere model simulation of the impact of a sudden stratospheric warming on thermosphere dynamics and electrodynamics. *Journal of Geophysical Research*, *115*, A00G08. https://doi.org/10.1029/2010JA015524

Fuller-Rowell, T. J., Akmaev, R. A., Wu, F., Anghel, A., Maruyama, N., Anderson, D. N., et al. (2008). Impact of terrestrial weather on the upper atmosphere. *Geophysical Research Letters*, *35*, L09808. https://doi.org/10.1029/2007GL032911

Fuller-Rowell, T. J., Codrescu, M. V., & Forbes, J. M. (1997). Neutral density specification using first principle models: Semi-annual variations and storms. In F. R. Hoots, et al. (Eds.), *Astrodynamics 1997, Adv. Astronaut, Sci. Ser.* (Vol. 97, pp. 565–581). Springfield, VA: Am. Astronaut. Sci.

Fuller-Rowell, T. J., & Evans, D. S. (1987). Height-integrated Pedersen and Hall conductivity patterns inferred from the TIROS-NOAA satellite data. *Journal of Geophysical Research*, *92*, 7606–7618. https://doi.org/10.1029/JA092iA07p07606

Goncharenko, L. P., Coster, A. J., Chau, J. L., & Valladares, C. E. (2010). Impact of sudden stratospheric warmings on equatorial ionization anomaly. *Journal of Geophysical Research*, *115*, A00G07. https://doi.org/10.1029/2010JA015400

Hagan, M. E., Maute, A., Roble, R. G., Richmond, A. D., Immel, T. J., & England, S. L. (2007). Connections between deep tropical clouds and the Earth's ionosphere. *Geophysical Research Letters*, *34*, L20109. https://doi.org/10.1029/2007GL030142

Huang, C. S., Foster, J. C., & Kelley, M. C. (2005). Long-duration penetration of the planetary electric field to the low-altitude ionosphere during the main phase of magnetic storms. *Journal of Geophysical Research*, *110*, A11309. https://doi.org/10.1029/2005JA011202

Immel, T. J., Sagawa, E., England, S. L., Henderson, S. B., Hagan, M. E., Mende, S. B., et al. (2006). Control of equatorial ionospheric morphology by atmospheric tides. *Geophysical Research Letters*, *33*, L15108. https://doi.org/10.1029/2006GL026161

Khadka, S. M., Valladares, C. E., Sheehan, R., & Gerrard, A. J. (2018). Effects of electric field and neutral wind on the asymmetry of equatorial ionization anomaly. *Radio Science*, *53*, 683–697. https://doi.org/10.1029/2017RS006428

Kikuchi, T., Lühr, H., Kitamura, T., Saka, O., & Schlegel, K. (1996). Direct penetration of the polar electric field to the equator during a DP 2 event as detected by the auroral and equatorial magnetometer chains and the EISCAT radar. *Journal of Geophysical Research*, *101*, 17,161–17,173. https://doi.org/10.1029/96JA01299

Lindzen, R. S. (1981). Turbulence and stress owing to gravity wave and tidal breakdown. *Journal of Geophysical Research*, *86*, 9707–9714. https://doi.org/10.1029/JC086iC10p09707

Liu, H.-L., Yudin, V. A., & Roble, R. G. (2013). Day-to-day ionospheric variability due to lower atmosphere perturbations. *Geophysical Research Letters*, *40*, 665–670. https://doi.org/10.1002/grl.50125

Mannucci, A. J., Tsurutani, B. T., Iijima, B. A., Komjathy, A., Saito, A., Gonzalez, W. D., et al. (2005). Dayside global ionospheric response to the major interplanetary events of October 29–30, 2003 "Halloween Storms,". *Geophysical Research Letters*, *32*, L12S02. https://doi.org/10.1029/2004GL021467

Maruyama, N., Richmond, A. D., Fuller-Rowell, T. J., Codrescu, M. V., Sazykin, S., Toffoletto, F. R., et al. (2005). Interaction between direct penetration and disturbance dynamo electric fields in the storm-time equatorial ionosphere. *Geophysical Research Letters*, *32*, L17105. https://doi.org/10.1029/2005GL023763

McCormack, J. P., Eckermann, S. D., Siskind, D. E., & McGee, T. J. (2006). CHEM2D-OPP: A new linearized gas-phase ozone photochemistry parameterization for high-altitude NWP and climate models. *Atmospheric Chemistry and Physics*, *6*(12), 4943–4972. https://doi.org/10.5194/acp-6-4943-2006

Millward, G. H., Müller-Wodrag, I. C. F., Aylward, A. D., Fuller-Rowell, T. J., Richmond, A. D., & Moffett, R. J. (2001). An investigation into the influence of tidal forcing on F region equatorial vertical ion drift using a global ionosphere-thermosphere model with coupled electrodynamics. *Journal of Geophysical Research*, *106*, 24,733–24,744. https://doi.org/10.1029/2000JA000342

Richmond, A. D. (1995). Ionospheric electrodynamics using magnetic apex coordinates. *Journal of Geomagnetism and Geoelectricity*, *47*, 191–212. https://doi.org/10.5636/jgg.47.191

Richmond, A. D., & Maute, A. (2013). Ionospheric electrodynamics modeling, in modeling the ionosphere-thermosphere system. In J. Huba, R. Schunk, & G. Khazanov (Eds.), *Geophysical Monograph Series* (Vol. 201, pp. 57–71). Washington, DC: American Geophysical Union. (also published online in 2014 by John Wiley, Chichester, U. K. https://doi.org/10.1002/9781118704417.ch6

Rishbeth, H., & Mendillo, M. (2001). Patterns of F_2-layer variability. *Journal of Atmospheric and Solar-Terrestrial Physics*, *63*(15), 1661–1680. https://doi.org/10.1016/S1364-6826(01)00036-0

Scherliess, L., & Fejer, B. G. (1999). Radar and satellite global equatorial F region vertical drift model. *Journal of Geophysical Research*, *104*, 6829–6842.

Solomon, S. C., & Qian, L. (2005). Solar extreme-ultraviolet irradiance for general circulation models. *Journal of Geophysical Research*, *110*, A10306. https://doi.org/10.1029/2005JA011160

Swinbank, R., & Ortland, D. A. (2003). Compilation of wind data for the Upper Atmosphere Research Satellite (UARS) Reference Atmosphere Project. *Journal of Geophysical Research*, *108*(D19), 4615. https://doi.org/10.1029/2002JD003135

Tsurutani, B. T., Verkhoglyadova, O. P., Mannucci, A. J., Saito, A., Araki, T., Yumoto, K., et al. (2008). Prompt penetration electric fields (PPEFs) and their ionospheric effects during the great magnetic storm of 30–31 October 2003. *Journal of Geophysical Research*, *113*, A05311. https://doi.org/10.1029/2007JA012879

Wang, H., Fuller-Rowell, T. J., Akmaev, R. A., Hu, M., Kleist, D. T., & Iredell, M. (2011). First simulations with a whole atmosphere data assimilation and forecast system: The January 2009 major sudden stratospheric warming. *Journal of Geophysical Research*, *116*, A12321. https://doi.org/10.1029/2011JA017081

Weimer, D. R. (1995). Models of high-latitude electric potentials derived with a least error fit of spherical harmonic coefficients. *Journal of Geophysical Research*, *100*(19), 595–19,607.